



Dynamics of sand response to rapid penetration by rigid projectiles

Mehdi Omidvar¹ · Joseph Dinotte¹ · Louis Giacomo¹ · Stephan Bless² · Magued Iskander²

Received: 29 December 2023 / Accepted: 14 May 2024 / Published online: 22 June 2024
© The Author(s), under exclusive licence to Springer-Verlag GmbH Germany, part of Springer Nature 2024

Abstract

The response of dry sand to rapid penetration by a rigid projectile is investigated through a series of high-speed penetration experiments. A ballistic range is used to vertically launch cylindrical projectiles and a scaled version of a 155 mm M107 projectile at impact velocities of approximately 200 m/s into sand targets. A photon Doppler velocimeter is used to track projectiles from impact to rest in the soil target. Data collected from the experiments include the evolution of the cavity crown along with displacement, velocity, and acceleration time history. Analysis of the results reveal that the soil bulk density has a major role in penetration resistance at high relative densities. The role of bulk density diminishes at lower relative densities. Furthermore, the shape of the projectile nose has limited influence on the penetration response, due to the formation of a kernel of crushed sand at high velocities. The crushed sand kernel, known as the false nose, has a curved surface, and it can be approximated as a cone with a 60° apex angle. Only projectiles with a nose sharper than this value affect penetration resistance, while blunter noses effectively behave as 60° cones due to the formation of the false nose. A phenomenological equation of penetration resistance comprising inertial and frictional bearing resistance is used to describe the penetration response and predict the depth of burial (DoB) of the projectile in the soil target with reasonable accuracy.

Keywords Projectile Penetration · Depth of Burial · Unexploded Ordnance · Impact · Phenomenology · Poncelet

1 Introduction and Background

Interest in the study of rapid projectile penetration in soils dates back to Robins [1] and the design of military fortresses. The problem has been more extensively studied over the past several decades, with a wide range of civilian and military applications. Poncelet [2] derived equations based on a force argument that equates the forces on the projectile to the resistance in the soil target. The resulting equations have been widely employed in analysis of soils subject to rapid penetration [3–7], among others. Several revisions and improvements to the basic equations have been suggested in the literature [8–10]. Parallel developments in predicting dynamic penetration response in soils were made

by adopting cavity expansion solutions [11, 12]. A purely empirical approach to the problem was also studied at Sandia National Laboratories, which followed a large number of full-scale experiments in a range of soil sediments. The resulting empirical equations were the culmination of nearly a decade of field testing, and led to the widely used equations by Young [13], which correlates depth of burial (DoB) with soil and projectile parameters. A number of improvements and additions have been made to these equations [14].

In recent years, renewed interest in the study of projectile penetration in soils has stemmed from both civilian and military applications. In particular, the need for identification and remediation of buried unexploded ordnance (UxO) resulting from munitions development at Formerly used Defense Sites (FUDS) as well as their wartime deployment has motivated a number of studies [15], including the present work. There are over 5400 such sites within the US alone, and numerous similar sites internationally. An initial estimate of likely DoB of various ordnance within the cleanup depth can significantly aid planning and execution of cleanup efforts at these sites. A number of UxO detection technologies exist, each of which is capable of detecting ordnance to a certain depth below the ground surface. Thus,

✉ Mehdi Omidvar
omidvar@manhattan.edu

¹ Civil and Environmental Engineering Department, Manhattan College, Riverdale, NY, USA

² Civil and Urban Engineering Department, New York University, New York, NY, USA

an initial estimate of the DoB is required so that appropriate technologies can be deployed for detection. This is particularly important given the large size of some cleanup sites. Estimates of the DoB are often made using empirical and semi-analytical methods. These methods are developed and calibrated using penetration data. Such data are difficult and costly to acquire. The central objective of the present study was to produce high-fidelity data for development of predictive models for the DoB of UxO in sandy soils.

Methods to resolve the velocity of a projectile during penetration in a soil target include time of arrival screens [10, 16], high-speed imaging [17–19], embedded accelerometers [20, 21], flash X-ray [22], refractive index matching techniques [23–27], quarter space methods [28] and Photon Doppler velocimetry [29, 30]. Each of the above methods has advantages and disadvantages and is suited for a particular experimental configuration. PDV is increasingly used in scientific investigation to track motion from several m/s to > 10 km/s, in ballistic events such as shock physics and high-strain rate testing of solids [31]. It is best used in single event measurements, where materials are destroyed or irreversibly modified, such as explosive detonation testing or ejecta studies, and can be used to measure velocities of numerous objects simultaneously.

In this study, impact experiments on various sand targets are conducted to obtain high-resolution, precise, non-intrusive measurement of velocity during projectile penetration in sand targets. The motion of the projectile from impact to rest in soil targets was measured using a Photon Doppler velocimeter (PDV). The approach relies on the Doppler shift in coherent laser light waves to resolve the velocity–time history of a moving projectile. Comparison of the frequency content of the laser light before and after reflection from the projectile is used to find the instantaneous projectile velocity. The penetration data are used to develop a phenomenological model for prediction of DoB in sand deposits. In the next sections, details of the experimental setup, soil target preparation, and PDV measurements are presented. The high-fidelity data obtained in the present work are used to gain insight into the complex soil-projectile interactions that occur at various stages of soil penetration. Improved Poncelet model predictions are developed from a phenomenological analysis of the data.

2 Experimental Setup

The majority of ballistic experiments in the literature involve horizontally launching projectiles into soil targets. This presents a problem when studying penetration resistance of granular materials, since the stress–strain properties of these soils are depth dependent, and the strength of most natural

soil deposits vary with depth in the ground. Furthermore, in weaker soils the cavity formation and collapse may be asymmetric in a horizontal configuration, which may affect the penetration mechanics of the soil. It is therefore important to capture this depth-dependence in developing predictive models, particularly those intended for engineering applications. Therefore, a vertical projectile launcher was designed in this study to launch projectiles into sand targets.

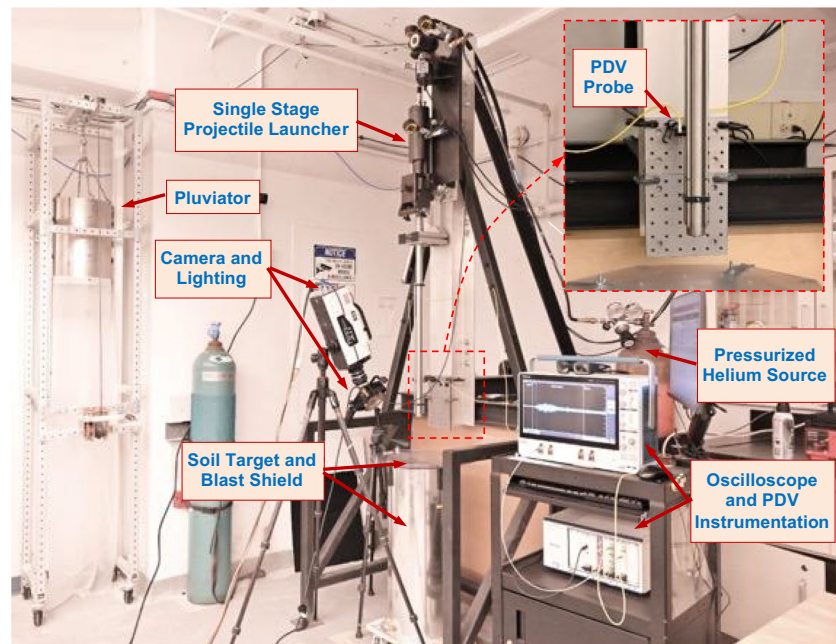
2.1 Launcher and Soil Properties

The launcher used to propel projectiles into soil targets was a custom-made single-stage gas gun with a very fast valve (*Sydor Technologies*). The launcher barrel was 1.22 m long with a 14.40 mm inner diameter and a 32.5 mm outer diameter (Fig. 1). The launcher was triggered electrically using a fast-acting electro-pneumatic solenoid. Dry compressed air was supplied to the solenoid at a regulated operating pressure of 8 bar to operate the solenoid valve, once an electrical signal opened the solenoid pilot valve. A free-floating shuttle valve allowed for abrupt release of pressurized helium gas into the barrel, thereby rapidly accelerating the projectile to the desired muzzle velocities. The sudden release of gas was critical in achieving high muzzle velocities. The launcher was operated at a helium pressure of 35–70 bar, corresponding to an impact velocity in the range of 150–200 m/s [32].

The main projectile used in the ballistic experiments was a circular cross-section rod with a conical nose, having a diameter of 14.3 mm, and a length-to-diameter ratio (L/D) of 6.14. The projectile was precision-machined from T6061 aluminum. Several conical nose angles with apex angles ranging from 30°–120° were used in excursion tests; the mass of all projectiles was kept constant at 34.5 g. Additionally, a replica-scaled version of the commonly used 155 mm M107 artillery projectile with a scale factor of 0.09, precision-machined from titanium, was employed in a number of experiments to relate the findings of the study to practical UxO cleanup applications. Projectiles were held in the launcher breech prior to launch using 2-mm wide double-sided tape, such that the tape temporarily adhered to the projectile and the inside wall of the gun breech before experiments [33]. The tape sheared off upon launching the projectile, thereby ensuring that the PDV laser light path was not obstructed during experiments.

A rigid steel frame was designed to support the launcher and its anticipated recoil. The frame was bolted into the lab floor to ensure sufficient rigidity during ballistic experiments. A 2.2 m long aluminum I-beam was attached to the frame and used to support the launcher and to provide adequate space and mounting options for optical and magnetic instrumentation. The frame was painted matte black to limit the reflection of laser light during experiments. A blast shield was manufactured from polycarbonate and was placed over the soil target

Fig. 1 Vertical ballistic range used to launch projectiles in sand targets



chamber in order to prevent the exhaust gas blast emptied behind the projectile from affecting the soil target surface.

Soil targets were produced from dry Ottawa sand, passing sieve No. 50 and retained on sieve No. 80, housed in cylindrical barrels. The d_{50} of the Ottawa sand, defined as the diameter corresponding to 50% finer by weight, was 0.3 mm. The barrels were made of 3.2 mm thick aluminum and were 0.76 m deep with a 0.31 m diameter. Soil targets with bulk densities of 1.82, 1.75, 1.65, and 1.57 g/cm³ were prepared by means of dry pluviation. These four soil densities corresponded to relative densities of 95%, 81%, 60%, and 41%, respectively. Dry density was measured by placing 75 mm diameter cylindrical containers within the target drum during pluviation. The density standard deviation of the 1.82, 1.75, 1.65, and 1.57 g/cm³ samples were 0.01, 0.03, 0.01, and 0.02 g/cm³, respectively.

2.2 Velocity measurement using photon doppler velocimetry

High fidelity velocity–time histories of projectile penetration into soil targets were obtained using a PDV setup. The measurement technique employs the Doppler effect of reflected laser light waves to resolve high velocities of moving objects.

Laser light having a frequency f_0 , when reflected from a moving source, will have a Doppler shifted frequency, f_D . Combining the Doppler-shifted light and the original unshifted laser light creates a new signal, known as the beat signal, the frequency of which is related to the instantaneous velocity, v , of the moving object, as follows [29, 31]:

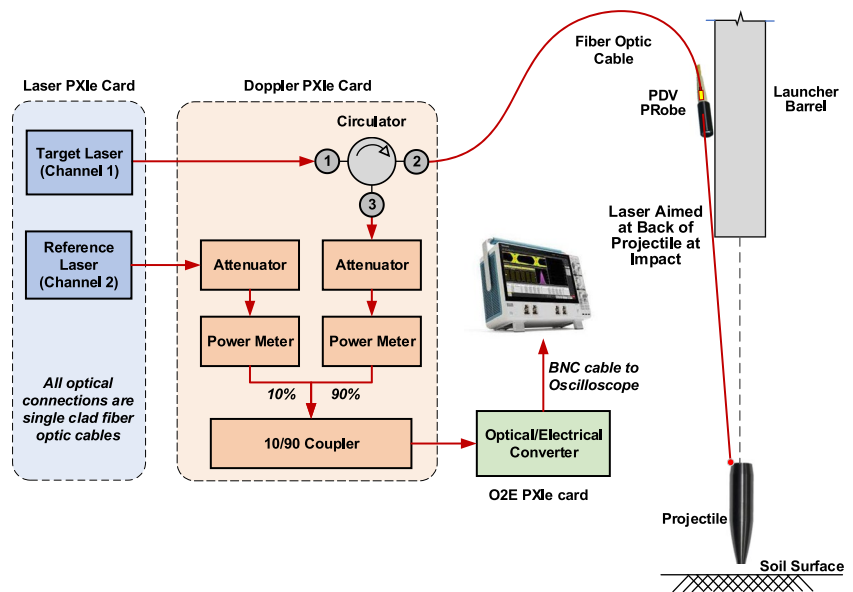
$$f_B = f_D - f_0 = f_0 \left| \frac{2v}{c} \right| \quad (1)$$

The beat signal can then be used to find the time-resolved velocity of the moving object, in this case, the projectile, $v(t)$, as $|v(t)| = 0.5f_B \lambda_0$. It is advantageous in making these velocity measurements to utilize a second reference laser having a small frequency difference compared to the original unshifted laser light. The frequency of the original unshifted light used in the experiment is then known as the target frequency, f_T , and the frequency of the reference laser light is known as the reference frequency, f_R . The resulting setup is known as a frequency shifted PDV, and it has the advantage that a beat signal can be generated from combining the two lasers, even when the object is not moving. In contrast, when using a single laser, the beat signal essentially vanishes as the object approaches zero velocity. As a result, low velocity movement is better captured using the latter configuration. The frequency of the beat signal is therefore calculated as

$$f_B = \left| f_T - f_R - \frac{2v(t)}{\lambda_T} \right| \quad (2)$$

A frequency-shifted PDV setup was utilized in this study, the components of which are schematically shown in Fig. 2. The target laser is directed through an optical circulator and is then directed to a probe, which in turn emits light at the moving projectile. The Doppler shifted light is reflected from the projectile back to the probe, and is combined with the unshifted target laser light in the

Fig. 2 Frequency shifted PDV configuration



circulator. The reference and Doppler-shifted laser lights are then combined at a rate of 10% and 90%, respectively, to produce the beat signal. The optical beat signal is passed through a converter which converts optical signals to electric signals. A fast oscilloscope is then used to resolve the frequency of the beat signal, from which the velocity of the projectile can be extracted, according to Eq. (2).

The PDV setup designed in this study comprised a laser and PDV optical components housed in a PXIe chassis (NI PXIe-1078). A PXIe controller card was used to interface and operate the following components on the chassis. The reference laser was operated at a wavelength of 1550 nm, and the target laser was upshifted such that a baseline beat frequency of approximately 0.3–0.5 GHz was produced in all shots. An optical-to-electrical converter was used to convert the optical beat signal to an electric signal, which was then analyzed in a fast oscilloscope (*Tektronix 6-Series Mixed Signal MSO64*).

Optical probes were strategically placed adjacent to the barrel muzzle to direct light to the projectiles during experiments. An *Oz Optics* collimated probe (LPC-01–1300/1550–9/125-S-0.5–2.61CL-40-3A-3.4) was used to direct light at the back of the projectile. Highly reflective retroreflective tape (*Telmechanique XUZB11*) was placed on the back of the projectiles to redirect light back to the probe for PDV analysis. The probe line of sight was selected such that it resulted in light reflecting back from the projectile to the probe over a penetration distance of approximately 220 mm following impact on the soil surface. In some experiments, the signal was lost in late stages of penetration when either (1) the projectile deviated from the vertical trajectory, or (2) if it penetrated deeper than the maximum depth of 220 mm. Precise alignment was achieved using an infrared-sensitive detector cards and visible lasers, details of which were described by [29].

2.3 Analysis of PDV Signals

PDV signals are analyzed in four main steps. The beat signal is first divided into finite analysis windows; the windows utilized in this study had 1,024 data points. A short time Fourier transform (STFT) of this window of the beat signal is computed by first multiplying the data by a window function. The process is then repeated for the next time window containing the same number of data points (1,024 in this case), until the entire dataset is covered from projectile impact to rest. Plotting the power spectrum for each window as a function of time results in a frequency spectrum. The peak of the power spectrum corresponds to the beat signal from the projectile, and it has the largest power in the spectrum. This frequency can then be used to compute the instantaneous velocity of the projectile using Eq. (2). The aforementioned calculations were carried out in MATLAB using the open-source code SIRHEN (*Sandia Infrared Heterodyne Analysis*) [34].

PDV signals were smoothed using a Savitsky-Golay algorithm [29]. Single differentiation of the data resulted in acceleration-time history. Similarly, the velocity-time data were integrated to obtain the penetration-time response of the projectile. The PDV measurements produced highly repeatable results, as shown in Fig. 3. Experiments were repeated for projectiles penetrating at an impact velocity of 200 m/s into dry sand with two bulk densities of 1.65 g/cm³ and 1.82 g/cm³. Nearly identical velocity-time histories were obtained from both repeat experiments. No additional effort was made to further quantify uncertainty and error, given the high degree of repeatability observed.

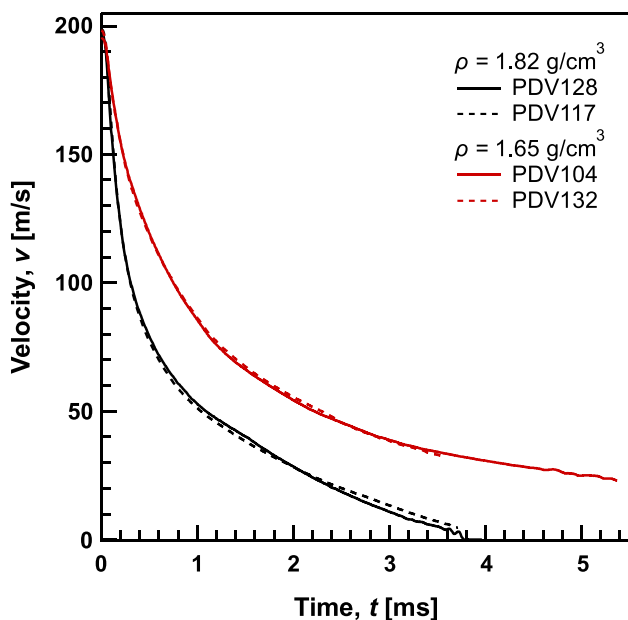


Fig. 3 Repeatability experiments shown for penetration of conical nose projectile in sand with densities of 1.82 g/cm³ and 1.65 g/cm³

3 Experimental Results

3.1 General observations

Ballistic experiments were carried out to investigate the role of the soil target and projectile properties on the penetration resistance of sand. Parameters considered were soil target bulk density as well as projectile mass and nose shape. Impact velocities of 150 and 200 m/s were investigated. The

lower velocities were used to demonstrate general response using a high-speed camera, while the higher velocity tests were used for phenomenological modeling. The latter experiments had a greater number of data points at high velocities, which allowed for more accurate modeling and predictions. The ballistics experiments conducted are summarized in Table 1. Velocity–time histories were obtained using the PDV setup described previously. Signals were subsequently smoothed and differentiated to produce acceleration–time histories. Single integration of the velocity–time history also produced penetration–time histories. Projectiles were carefully exhumed following each experiment to measure the depth of burial (DoB) and tilt at this depth from the vertical axis.

High-speed images obtained from a projectile impacting dense dry sand at an impact velocity of 150 m/s are shown in Fig. 4. Images were captured with an *NAC HX5* camera operating at 10 kHz. In addition to revealing soil–projectile interactions at impact and the initial phase of penetration, the high-speed images provided a tool to investigate potential issues with experiments, including pre-impact angle of attack, loss of signal, and gas blast interference with soil response. The velocity–time history of penetration is shown in the figure, along with high-speed images corresponding to one-diameter penetration increments. It can be seen that impact of the projectile onto the soil surface creates a cavity through which the projectile afterbody penetrates. The cavity produced upon impact evolves during subsequent stages of projectile embedment and deeper penetration. Inspection of the cavity evolution over time suggests that the soil is in contact with the projectile primarily along its nose, and that separation occurs between the soil and the projectile at the end of the projectile nose. The shank of the projectile

Table 1 Soil target and projectile parameters along with Poncelet parameters

Shot ID	Impact Velocity (m/s)	Projectile Properties		Soil Density (g/cm ³)	Depth of Burial (mm)	Projectile Tilt at DoB (°)	Incremental Poncelet Parameters	
		Mass (g)	Nose Shape				C	R (kPa)
PDV 76	203.4	34.5	60° Cone	1.82	147	12	2.18	1002
PDV 117	198.5			1.82	161	15	-	-
PDV 128	197.8			1.82	159	10	-	-
PDV 107	196.5			1.75	239	22	1.33	575
PDV 104	194.9			1.65	380	15	0.93	349
PDV 132	198.2			1.65	381	26	-	-
PDV 80	203.1			1.57	376	24	0.93	349
PDV 86	201.2		30° Cone	1.82	190	16	1.59	1177
PDV 87	198.9		90° Cone	1.82	135	12	2.28	938
PDV 88	200.0		120° Cone	1.82	148	10	2.21	901
PDV 89	196.9		Blunt	1.82	139	13	2.27	850
PDV 14	152.1		Blunt	1.76	155	30	-	-
PDV 81	196.6	33.3	Ogive	1.82	240	30	0.94	1240

Fig. 4 Snapshots of blunt projectile penetrating dense sand. Markers delineate each diameter of projectile penetration

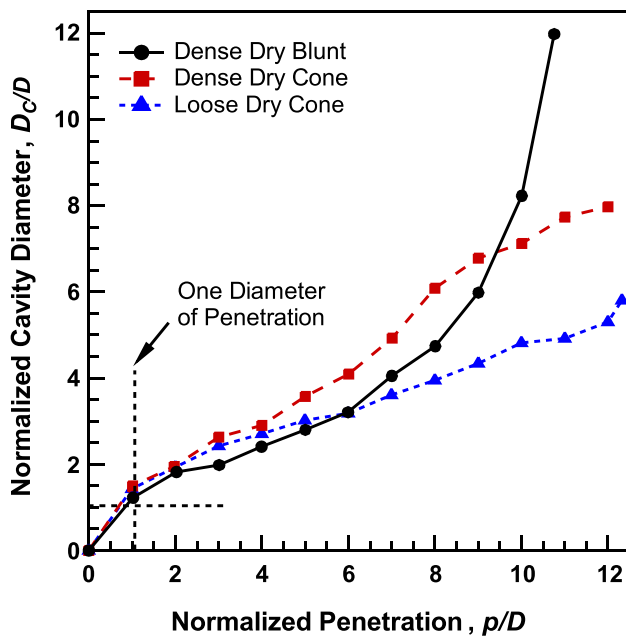
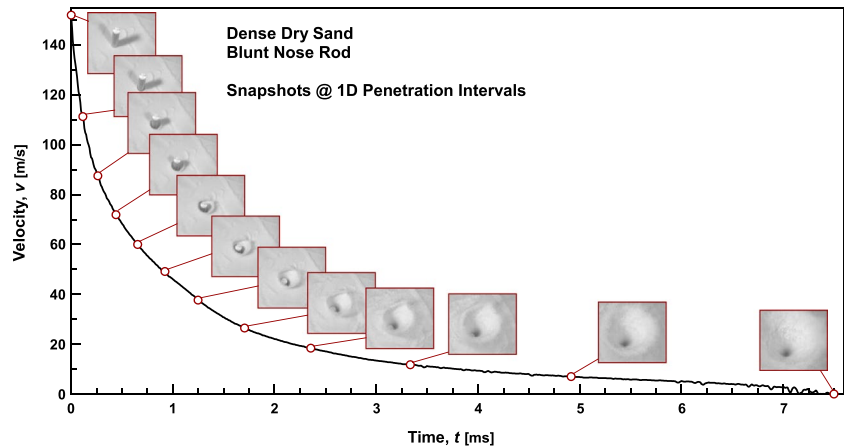


Fig. 5 Evolution of cavity crown diameter in shots into sand targets

travels inside the cavity and has little to no interaction with the soil for the majority of flight. The evolution of the cavity diameter, D_c , at its crown is shown in Fig. 5. It can be seen that (1) the cavity rim diameter grows nonlinearly for the blunt projectile, while the conical nose produces a smaller cavity; (2) the cavity diameter at full embedment is only slightly larger in loose sand compared to dense sand; (3) the cavity continues to expand once the projectile passes a given depth, and (4) the cavity diameter is larger than the projectile diameter following full embedment for all shots considered herein. In some experiments the projectile deviated marginally from its axis upon embedment. In these cases, the projectile afterbody interacted with the cavity walls, which led to stabilization of the projectile in further penetration. In shots using a blunt-nose projectile into dense sand targets, a

light flash was emitted at the soil-projectile impact surface as sand particles fractured and comminuted.

An important consideration in reduced scale impact and ballistic experiments is the possibility of wave reflections from sample boundaries. An impact-generated compression wave travels in the soil target and reflects from the boundaries. This compression wave can then interact with the projectile at later stages of penetration. These unwanted interactions can lead to extrinsic response. Studies have shown that lateral boundaries can significantly affect DoB and soil response to projectile penetration [35]. A soil target container-to-projectile diameter, known as the diameter ratio, of 3–15 has been utilized in high-speed testing into soil targets [10, 21, 36–38], and a diameter ratio of 40 or higher has been recommended for quasi-static loading to avoid boundary effects in reduced scale soil experiments [39]. A preliminary experimental campaign was carried out to identify potential boundary effects in this study. Two chamber diameters of 305 mm and 203 mm were used, corresponding to diameter ratios of 21.3 and 14.2, respectively.

Velocity–time, force–time, and velocity–penetration plots for a conical nose projectile penetrating into loose and dense sand targets with the diameter ratios are shown in Fig. 6. It is clear from the comparisons that the lateral boundaries affect the forces on the projectile during penetration, as well as the DoB. Closer inspection of the force–time histories reveals that projectiles experienced an abrupt increase in penetration resistance at a penetration time of approximately 1.0 ms and 0.5 ms in chambers with a diameter ratio of 21.3 and 14.2, respectively. This abrupt increase is the result of compression which emanated from the projectile upon impact onto the soil surface. These waves travelled through the soil, reflected back from the relatively high impedance chamber wall as a recompression wave, and converged back on axis, thus affecting projectile penetration response. The projectile penetration depth corresponding to the time of the wave arrival was used to find the trajectory of the compaction wave front, as shown in Fig. 6. The wave velocities

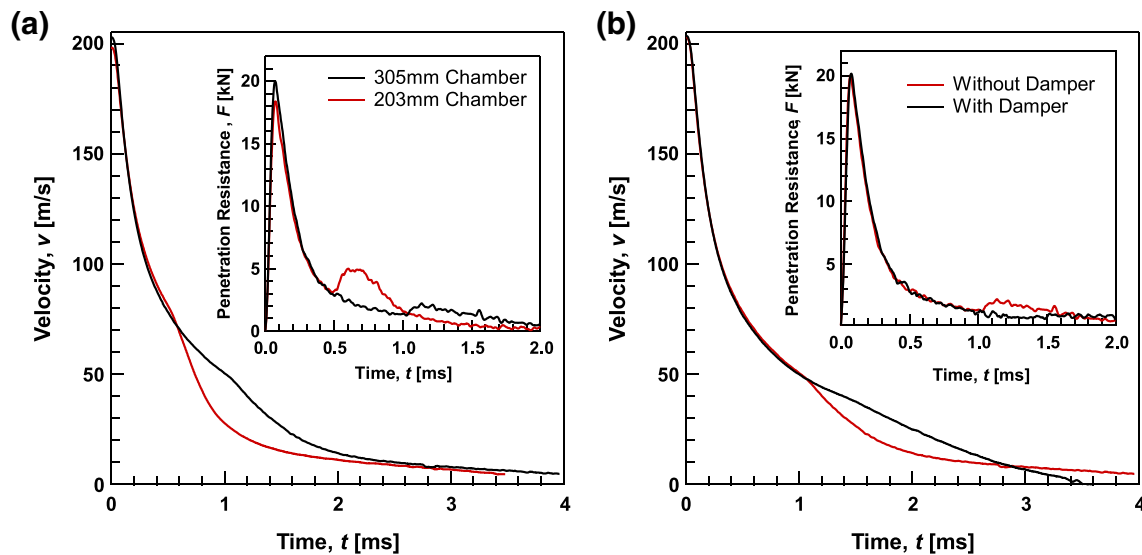


Fig. 6 Ballistic experiments into target chambers; **a** having diameter ratios of 14.2 and 21.3; **b** with and without damping material

found from this approach in target chambers with $14.2D$ and $21.3D$ diameters considered were 370 m/s and 300 m/s, respectively. The similarity between the two values further confirms that the abrupt penetration resistance observed in the force–time histories in Fig. 6 is due to boundary effects.

An average compaction wave propagation velocity of 335 m/s was used to determine the soil target chamber diameter required to completely eliminate boundary effects. A chamber diameter in excess of 2 m would be needed to fully eliminate boundary effects considering the penetration depths observed in this study. Such a prohibitively large chamber size would present a number of logistical challenges and would limit the number of experiments that could be carried out. Instead, effort was dedicated to reducing boundary effects by placing shock absorbing liners along the interior wall of the soil target chamber. Several lining materials were tested, and it was found that a liner made of fiber reinforced PVC effectively eliminated the majority of wave reflection into the soil target. Comparison of experiments in unlined and shock absorbing damper-lined soil target chambers is shown in Fig. 6, demonstrating the efficacy of the damper in reducing boundary effects. However, despite these improvements, minor boundary effects were still observed in some experiments, particularly in denser soil targets. These effects were identified where it was deemed that they interfered with the late-time projectile response.

3.2 Role of Soil Density

Results of ballistic experiments in dry sand at bulk densities ranging from 1.57 g/cm^3 to 1.82 g/cm^3 are shown in Fig. 7. Projectiles decelerated rapidly upon impact onto the soil

surface, reaching a peak deceleration at a penetration depth that corresponded to full nose embedment. Projectile deceleration decayed rapidly following this peak deceleration. All soil densities tested subsequently reached a comparable deceleration of approximately $2.5 \times 10^4 \text{ m/s}^2$ at a penetration time of 1.5 ms. The density comparison reveals that the soil bulk density only plays a major role in the DoB at higher densities. It appears that there is a threshold bulk density, at approximately 1.65 g/cm^3 , corresponding to a relative density of 60% for the Ottawa Sand tested, below which penetration resistance and DoB are not sensitive to soil density. Above this threshold DoB seems to linearly decrease with an increase in bulk density, as shown in Fig. 8. The DoB of the conical rod projectile was 133% or $15D$ deeper in the loosest sand compared to the densest sand target, while the DoBs of the two lowest densities, which differed in relative density by nearly 20%, were approximately the same.

An explanation for this varying level of sensitivity to bulk density can be provided by considering energy dissipation mechanisms during high velocity penetration into granular materials. As a projectile penetrates a soil target at high velocities, resistance to penetration occurs primarily as momentum transfer to soil particles. The frictional shear response of soils plays a secondary role in this regime. In high density soil targets, there is limited void space for the soil to move into, and the soil particles are kinematically constrained because of a large number of contact points. As a result, large stresses are generated in soil particles, which exceed their crushing strength, evidence of which is provided later in this study. Penetration resistance in this regime becomes highly sensitive to change in porosity, since it can significantly affect the magnitude of stress in the soil particles. In penetration of low-density granular soils, however,

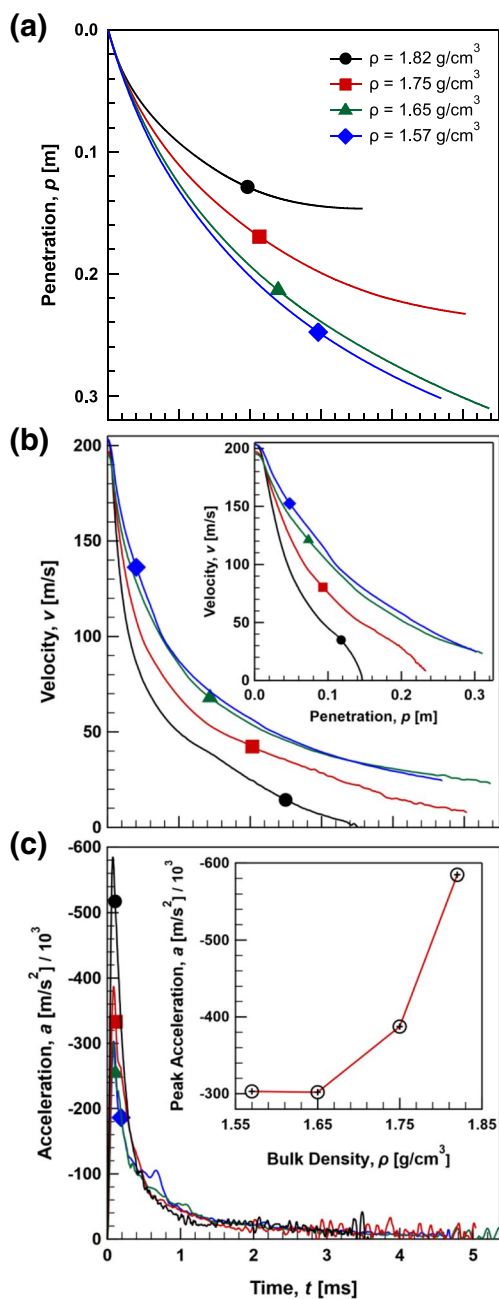


Fig. 7 Comparison of projectile penetration into dense and loose dry sand; **a** penetration-time history; **b** velocity-time history; **c** acceleration-time history. Inset of **c** show peak deceleration vs. bulk density

momentum transfer from the projectile to the soil particles can occur with much less interaction between sand particles, since there are relatively large voids into which the soil particles can flow. As a result, small changes in porosity do not materially affect soil resistance to penetration at high velocities.

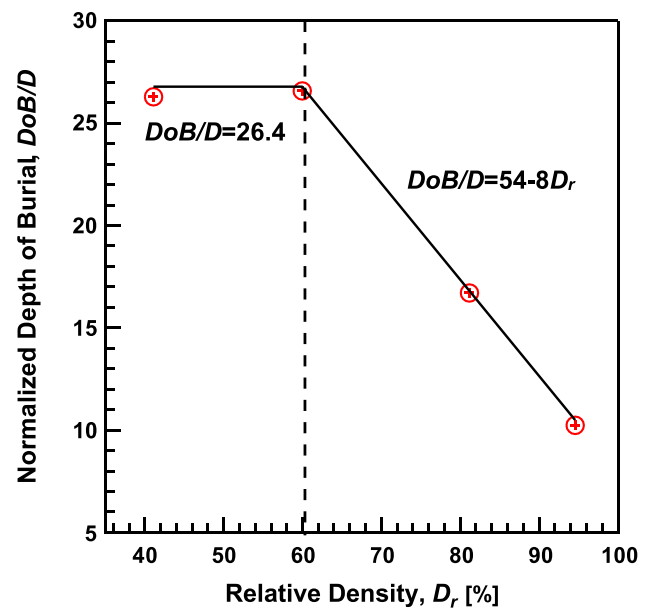


Fig. 8 Depth of Burial (DoB) as a function of relative density (D_r)

3.3 Role of Nose Shape

The role of projectile nose shape on soil resistance to rapid penetration was investigated by launching projectiles with conical noses at different angles, including 30° , 60° , 90° , and 120° , along with a blunt nose projectile and a scaled replica of an M107 artillery round into dry sand targets having a density of 1.82 g/cm^3 (Fig. 9). It can be seen that the peak penetration resistance is highest in the case of the blunt projectile, and it decreases as the nose becomes sharper. The M107 projectile has the lowest penetration resistance. In all cases, the peak penetration resistance occurred corresponded to full nose embedment, as shown in the inset of the figure. It is noteworthy that the values reported in Fig. 9a were corrected for the time required for compressive waves generated at the nose of the projectile to reach its back end, where the PDV measurements were made. The depth of burial of all projectiles were comparable to each other, with the notable exception of the 30° conical nose and M107 projectiles, which exhibited significantly deeper depths of burial of approximately $3.2D$ and $6.8D$ deeper, respectively, than the average depth of burial of the other projectiles. The data suggest that nose shape significantly affects penetration resistance only if the nose apex angle is smaller than a threshold value, which appears to be approximately 60° for the projectiles and soils tested.

The observed nose shape effects can be attributed to particle crushing in high velocity penetration of densely packed sand. During projectile embedment in the soil, the stresses generated immediately ahead of the projectile exceed its crushing strength, resulting in intense particle crushing,

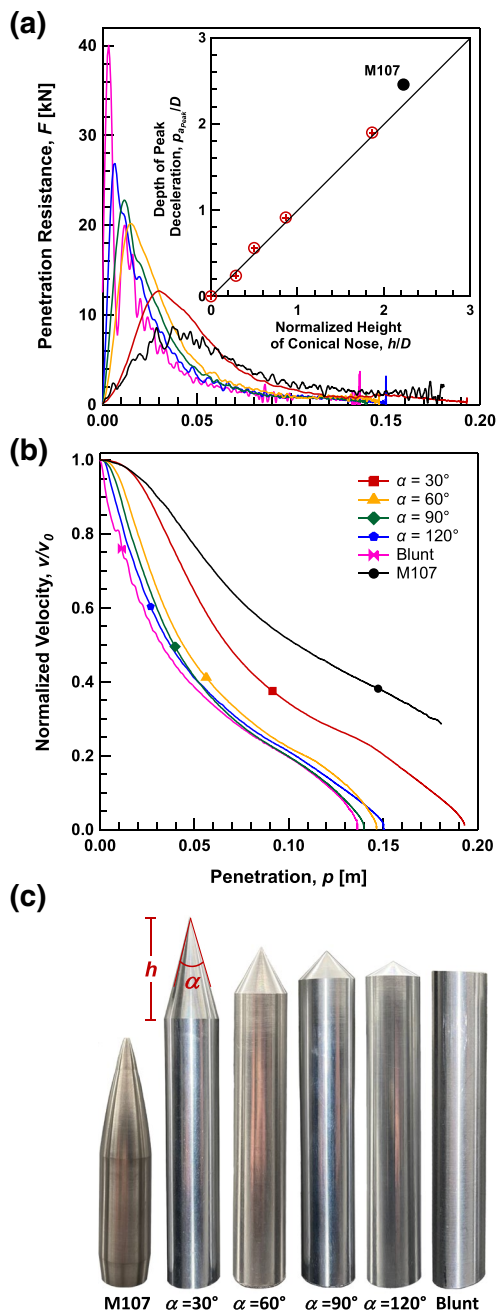


Fig. 9 Comparison of projectiles with various cone angles penetrating dense sand; **a** penetration resistance as a function of penetration depth; **b** normalized velocity-penetration

known as comminution. As a result of this particle crushing, a kernel of highly compacted crushed sand forms ahead of the projectile. This crushed soil kernel, known as a false nose, remains attached to the projectile during subsequent penetration, and acts as an apparent nose for the projectile. Example of the false nose formed ahead of a blunt projectile and a 120° cone projectile are shown in Fig. 10. The exact shape of the kernel has been studied by several authors in

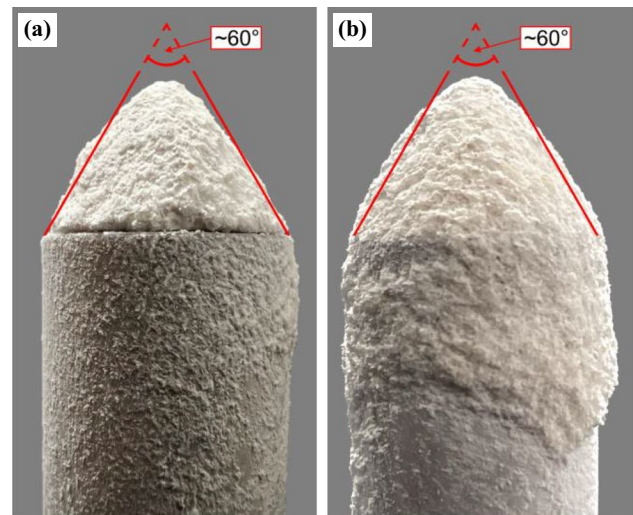


Fig. 10 Image of false nose found on the **a** blunt and **b** 120° conical nose projectiles during post mortem investigation

the literature [21, 24, 40, 41], and it can be approximated as a cone with a 60° apex angle for the soil tested. The false cone therefore mitigates the role of nose shape in subsequent penetration for projectiles with an initial nose angle greater than approximately 60°. The deceleration time histories in Fig. 9 are consistent with this behavior, where it can be seen that following peak deceleration, soil resistance in all projectiles except the 30° cone and the M107 projectile reduces to comparable values. However, initial projectile nose angles sharper than that of the false nose do not form a false cone. These projectiles penetrate more efficiently into the soil target, resulting in a significantly deeper DoB.

3.4 Role of Pore Saturation

A comprehensive understanding of phenomena leading to the observed differences in penetration resistance of dry and partially-saturated sand would require knowledge of pore pressures and mesoscale deformations at these velocities. Such data were not collected in this study, and their availability in the literature is limited. However, meso-scale deformation measurements and post mortem analysis of low velocity penetration tests by Omidvar et al. (2015) and Iskander et al. (2015) into refractive index-matched granular media can be used to glean possible mechanisms responsible for the observed macro scale response. These studies report the formation of an opaque region in penetration into refractive index transparent soils. This opaque region maybe attributable to cavitation of pore fluid. The timescale of particle movement, imposed by the projectile velocity, exceeds the timescale required for water flow through the pores. Consequently, very high negative pore water pressures are generated in this region, which rapidly reaches the

vapor pressure of the pore water and leads to cavitation. The role of water then is primarily to lubricate the soil contacts during this stage of inertial resistance to penetration. As the projectile slows toward the depth of burial, however, pore fluid cavitation is mitigated, and a combination of negative hoop strains and shear induced dilation leads to negative pore pressures that translate to elevated effective stresses in the soil contacts, resulting in greater penetration resistance.

4 Interpretation within phenomenological framework

The observations described above can be used to develop a phenomenological physical model of penetration into sandy soil targets. It can be assumed that a rigid projectile penetrating a soil target exerts a force to move the soil out of its path, the magnitude of which must be the equal to the force in the soil that decelerates the projectile. The resulting governing equation of penetration is based on Newton's second law of motion. In this approach, the net force acting on the projectile during soil penetration can be represented by a polynomial with varying orders of dependence on penetration velocity, as follows:

$$m \frac{dv}{dt} = mg - \alpha v^2 - \beta v - \gamma \quad (3)$$

where m is the projectile mass, v is the penetration velocity, g is the gravitational constant, and α , β , and γ , are resistance coefficients that depend on the properties of both the penetrator as well as the soil. Physically, the second term on the right-hand side of Eq. (3) is interpreted as an inertial resistance, the second third term is a viscous resistance, and the fourth term is a velocity-independent frictional bearing resistance. The contributions of the gravitational force and viscous resistance terms in Eq. (3) are often neglected in high velocity penetration.

The constant of the inertial term, α , can be found in terms of the soil and projectile properties by considering a mass of soil, dm , ahead of a projectile moving at a velocity, v , in the sand target. The projectile cross-sectional area is A and the soil bulk density is ρ . Over a time increment of dt , the projectile accelerates a mass of soil $dm = \rho dV = \rho z dA$ ahead of it to a velocity v , where V is the volume of the soil affected. The momentum transferred to the soil is therefore $dp = dm v = \rho dz A v$. The inertial forces resulting from changes in momentum over time can be written as $C \rho A v^2$, where C is a drag coefficient introduced to account for the imperfect transfer of momentum to the soil. The α term in Eq. (3) can therefore be approximated as $C \rho A$. The above derivation assumes frictionless collision at particle–particle and particle–projectile contacts. Assuming the role of friction can be decoupled from inertial forces, the bearing resistance

term γ can be superimposed as a force equal to RA , where R is the bearing stress and A is the projected cross-section area of the projectile. While R is generally a function of depth, it was approximated as a constant in the subscale experiments reported herein. R can be written as the sum of the stresses on the projectile nose and the frictional resistance along its shank. However, given that soil–projectile separation occurs at the end of the projectile nose at a wide range of velocities during high-velocity penetration into sand, it was assumed that R results only from the bearing stress ahead of the projectile nose. The resulting governing equation, known as the Poncelet equation, is then

$$-m \frac{dv}{dt} = C \rho A v^2 + RA \quad (4)$$

Solving Eq. (4) for velocity as a function of depth, and integrating the resulting equation yields the following equation for instantaneous penetration depth, z , as a function of impact velocity, v_0 , and instantaneous penetration velocity, v :

$$z = \frac{m}{2C\rho A} \ln \left(\frac{v_0^2 + \frac{R}{C\rho}}{v^2 + \frac{R}{C\rho}} \right) \quad (5)$$

The C and R values used in Eq. (5) are determined through curve-fitting to experimental velocity–penetration data. Setting the instantaneous velocity, v , in Eq. (5) to zero yields the depth of burial (DoB) of the projectile.

While the analytical solution to the Poncelet model provides a convenient means to describe the velocity–penetration response of projectiles in soil targets, it does not explicitly capture important physical phenomena in the soil during high velocity penetration, such as particle crushing and pore fluid pressure generation, among others. Instead, the terms C and R are used to capture the net effects resulting from these complex soil–projectile interactions.

Another shortcoming of Eq. (5) is that it ignores the variable projectile area during nose embedment. During this initial stage of penetration, the projected circular cross-section of the projectile increases from zero at impact to the area of the projectile shank at full nose embedment. The evolution of the projected area can be described as a function of penetration depth. Referring to Fig. 13, the projected area can be written as πr^2 or conical (Eq. 6) and ogive (Eq. 7) nose projectiles, where r is the depth-varying projected nose radius, found as follows:

$$r = \frac{z}{\tan\left(\frac{\alpha}{2}\right)} \quad (6)$$

$$r = \sqrt{(2R[CRH])^2 - (R\sqrt{4[CRH] - 1} - z)^2} + R - 2R[CRH] \quad (7)$$

where z is the penetration depth, R is the maximum radius of the projectile, α is the apex angle of the conical nose, and CRH is the caliber radius head ratio, and is defined as the ratio between the ogive radius and the diameter of the projectile. To facilitate the implementation of the depth varying cross-sectional area within the Poncelet framework, a finite difference version of Eq. (5) was implemented. The resulting equation for velocity as a function of depth is as follows:

$$v_{i+1} = v_i - \frac{C\rho A_i v_i^2 - RA}{mv_i} \Delta z \tag{8}$$

where v_i is the current velocity of the projectile, v_{i+1} is the velocity of the projectile after an increase in penetration, Δz , and A_i is the depth-varying cross-sectional area of the projectile. An example of fitting Eq. (8) to ballistic data is shown in Fig. 11 for a 30° conical nose penetrating dense dry sand. Also shown in the figure is a fit using Eq. (5). The depth corresponding to full nose embedment is marked in the figure. It can be seen that the nose embedment phase is captured accurately using the incremental implementation, while Eq. (5) produces significant error. Equation (8) was used to fit to the data reported in herein.

Predictions of the velocity-penetration behavior according to the Poncelet model of Eq. (8) are shown in Fig. 12 for a range of C and R values pertaining to sand. It can be seen that C generally determines the high-velocity response, while R controls the low velocity response and the DoB. This is particularly true for soils with higher drag coefficients. For example, at a drag coefficient of two, varying R from zero to 5 MPa has little bearing on the high velocity response down to approximately 50% of the impact velocity.

Fig. 11 Comparison of Poncelet fit with and without area correction during nose embedment in the soil

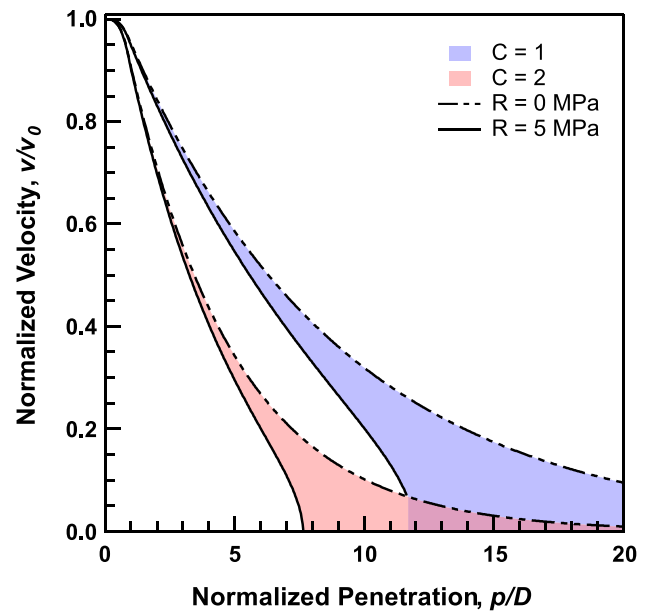
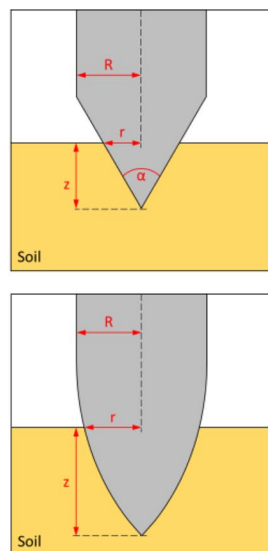
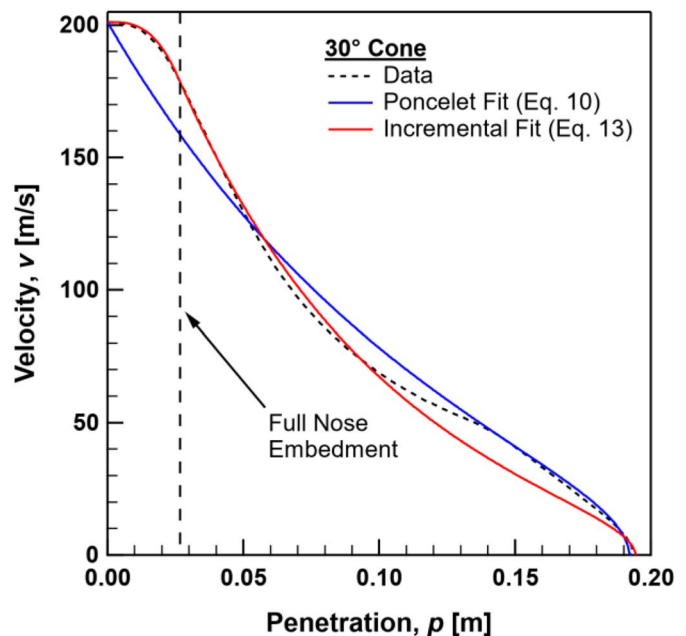


Fig. 12 Role of C and R in Eq. (8)

The role of R at high velocities increases as the drag coefficient decreases. Importantly, the model predicts infinite penetration depth for an R value of zero. That is, the projectile would penetrate infinitely in a material with no shear strength, such as water. In curve-fitting to penetration data, it was found that the best-fit values that minimized error produced R values approaching zero, and a resulting penetration depth that was unrealistically deep. In order to overcome this limitation, curve-fitting was carried out with the constraint that the predicted DoB could not deviate from the measured



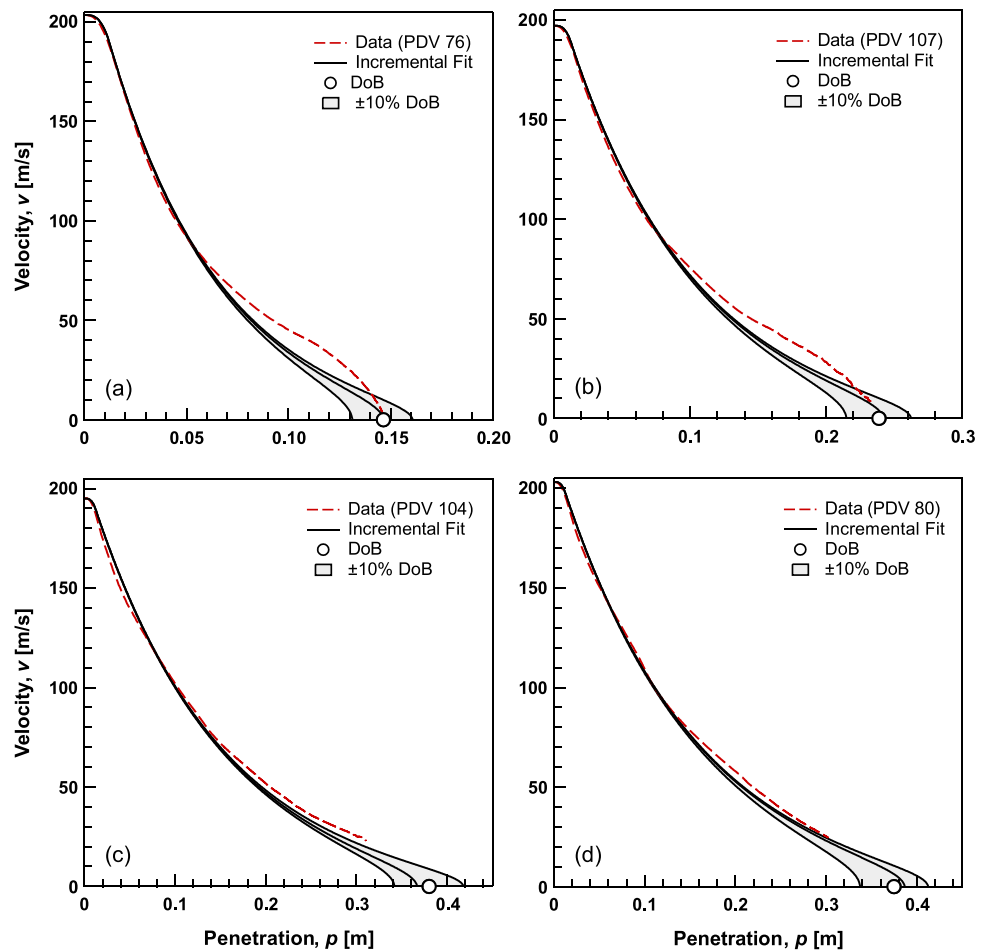
DoB by more than 10%. Subsequently, a regression analysis was performed using the computed R values to establish a relationship between R and bulk density. This relationship was then used to determine the R values presented in Table 1.

The results of fitting Eq. (8) to the ballistic data for dry sand at different bulk densities are presented in Fig. 13. The values obtained for C and R for all experiments reported in this study are also summarized in Table 1. C and R ranged from 0.9 to 2.3 and 300 to 1000 kPa for the densest and loosest soils tested, respectively. The fits to the data accurately capture high velocity penetration in all soils to a penetration velocity of approximately 80 m/s. It is evident from Fig. 13 that the Poncelet fits generally capture the high velocity data more accurately than the low velocity data. The deviation of the fits from the data may be attributed to one or several physical phenomena during penetration, two of which include the development of an angle of attack in the projectile at lower velocities, and a transition from penetration facilitated primarily by means of particle crushing to one of particle rearrangement. In postmortem examination of the soil targets, all projectiles were retrieved with an angle of attack and slight deviation from the vertical penetration

axis. The angle of attack ranged from 10–30°, and generally increased in looser soil targets. Development of an angle of attack and deviation from vertical penetration can trigger soil-projectile shank interactions, leading to changes in soil resistance to penetration.

The root cause of the development of an angle of attack at lower velocities is not well understood. The deviation may be related to changes in penetration mechanism as the projectile slows down. As discussed previously, high velocity penetration generates large pressures in the soil ahead of the projectile, which exceeds its crushing strength. Crushed particles ahead of the projectile are packed into the interstitial void spaces of adjacent particles, thereby facilitating further projectile penetration. As the projectile slows down, it reaches a critical velocity below which stresses fall below the crushing strength of the soil particles. Further penetration into the soil target is therefore facilitated primarily by particle rearrangement and movement outward from the path of the projectile. Studies of high velocity projectile penetration in soil targets have reported a trail of highly crushed sand along the path of the projectile from impact to velocities in the range of 80–100 m/s, below which the trail of crushed sand was no longer clearly visible [10, 16]. This transition in penetration

Fig. 13 Results of curve-fitting Eq. (8) to the ballistic data for penetration into soil targets having a bulk dry density of **a** 1.82g/cm³; **b** 1.75g/cm³; **c** 1.65g/cm³; **d** 1.57g/cm³



mechanism is related to the crushing strength, which is a function of the bulk density. Confined compression tests on quartz sand suggest that deformations at stresses above 25–30 MPa are almost entirely facilitated by particle crushing [42–44]. Penetration resistance as a function of velocity for the four bulk densities tested is shown in Fig. 14. It can be seen that all soils tested generate high pressures exceeding the crushing strength of sand. The crushing threshold of 25–30 MPa is also shown in the figure. The subtle transition occurs at different velocities for soils having different densities, increasing from 85 m/s in the densest sand to 140 m/s in the loosest sand. However, all of the transitions coincide at a common penetration resistance in the range of 3.5–4.5 kN, corresponding to an average stress of approximately 25 MPa. The transition velocities, delineated in Fig. 14, also correspond closely to the velocity where the Poncelet fit deviates from the data. This observation supports the hypothesis that there is a transition in penetration response of sand related to particle crushing.

The transition velocity discussed above likely marks the onset of development of angle of attack in the projectile, although experimental evidence to corroborate this hypothesis was not collected beyond the recorded tilt and off-axis position of recovered projectiles following experiments. PDV signals could only be retrieved from the back of the projectile if it remained nearly vertical during penetration. Development of significant angle of attack would move the back of the projectile outside the line of sight of the PDV signal. A PDV signal was obtained from all tests above the transition stress noted above, indicating that penetration was

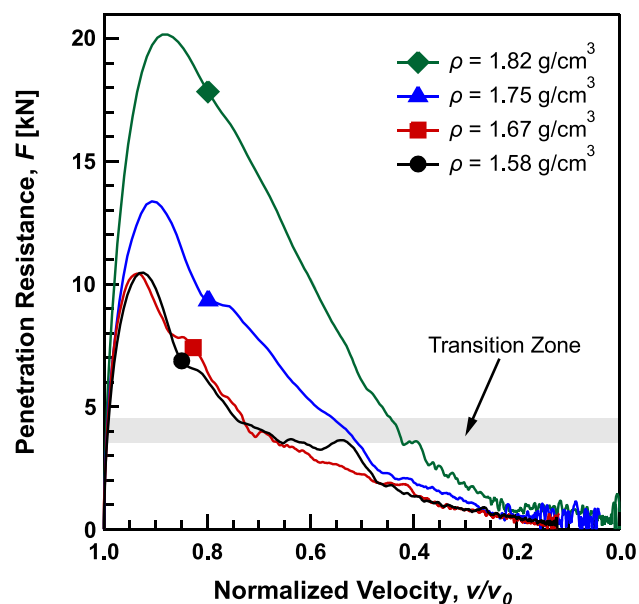


Fig. 14 Penetration resistance as function of velocity for penetration into soil densities of 1.82, 1.72, 1.65, and 1.57 g/cm³

near vertical above this transition stress. The developed tilt and off-axis drift is therefore attributed to penetration below the transition stress. Since the attached false nose forms at penetration velocities above the transition, it is expected that its shape will be symmetric on the projectile nose, which is corroborated by observations of retrieved false noses in this study.

Once an angle of attack develops in the projectile, additional resistance is introduced along the projectile shank as it interacts with the cavity walls. The center of pressure on the projectile moves away from nose as a result. If the center of pressure moves behind the center of mass, the shank-cavity interaction generates a restoring moment and corrects the projectile trajectory back to vertical penetration. This is believed to be the case in dense sand. In looser sands, the cavity force may not be large enough to move the center of pressure behind the center of mass. In this case, a destabilizing moment is generated on the projectile. As a result, the back of the projectile pushes deeper into the cavity wall, which in turn increases the force on the shank and moves the center of pressure farther back. This continues until the center of pressure moves behind the center of mass and further tilt is mitigated. Post mortem observations revealed that looser soil samples had larger tilt and off-axis drift, but the developed angle of attack did not lead to projectile instability and j-hooking. The extent of the soil-shank interaction and the resulting restoring forces is also a function of the projectile length. Longer projectiles are generally more stable than shorter ones for this reason. The M107 projectile with an L/D ratio of 4.54 had a greater angle of attack and deviation from vertical penetration compared to the conical nose projectile, which had an L/D of 6.14. In some cases, with penetration of shorter projectiles, development of angle of attack can lead to j-hooking and even an upward penetration trajectory, which mitigates further penetration into relatively loosely packed sand targets [45]. If this happens at higher velocities, it can potentially lead to development of an asymmetric false nose, although no such evidence was observed in this study.

Variation of C and R with bulk density is shown in Fig. 15. In addition to the best-fit values, the R values corresponding to 90% and 95% of the measured DoB are also shown in the figure. The soil response to projectile penetration is highly dependent on bulk density at high densities, whereas it is less sensitive to changes in density at low densities below a relative density of approximately 60%. Variation of C and R with projectile nose length is also shown in Fig. 16. It can be seen that C is generally not sensitive to nose length below an h/D ratio of 0.87 corresponding to a 60° conical nose. This is due to the formation of the false nose reported in previous sections. As the nose becomes sharper than the angle formed by the false nose, C significantly decreases. Projectiles penetrate deeper into the soil,

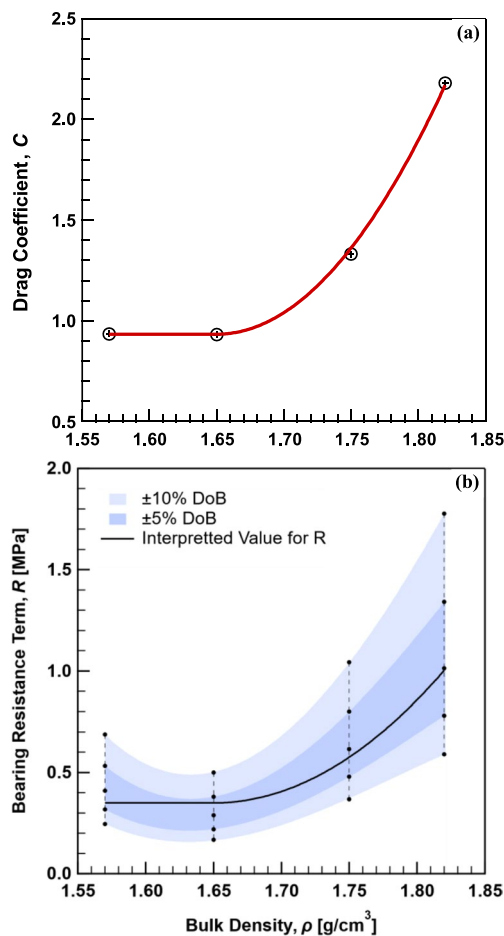


Fig. 15 Drag Coefficient and Bearing Resistance Term versus Bulk Density

resulting in slightly larger R values. The highest C of 2.27 was obtained for the blunt nose projectile, and the lowest C was found for the 30° cone nose. R values mostly increase as the nose length increases. The R value for M107 is not shown in the figure, since the projectile became unstable at low velocities.

5 Conclusions

The results of ballistic experiments in soil targets using conical nose projectiles and a scaled M107 artillery projectile were reported in this study. The experimental setup comprised a gas gun that was used to launch projectiles at impact velocities of approximately 200 m/s, and Photon Doppler velocimetry (PDV) instrumentation to track the projectile velocity during penetration. Sand targets with densities of 1.82, 1.75, 1.65, and 1.57 g/cm³ were prepared through dry pluviation. A frequency-shifted PDV configuration was designed in which two independent lasers light sources were

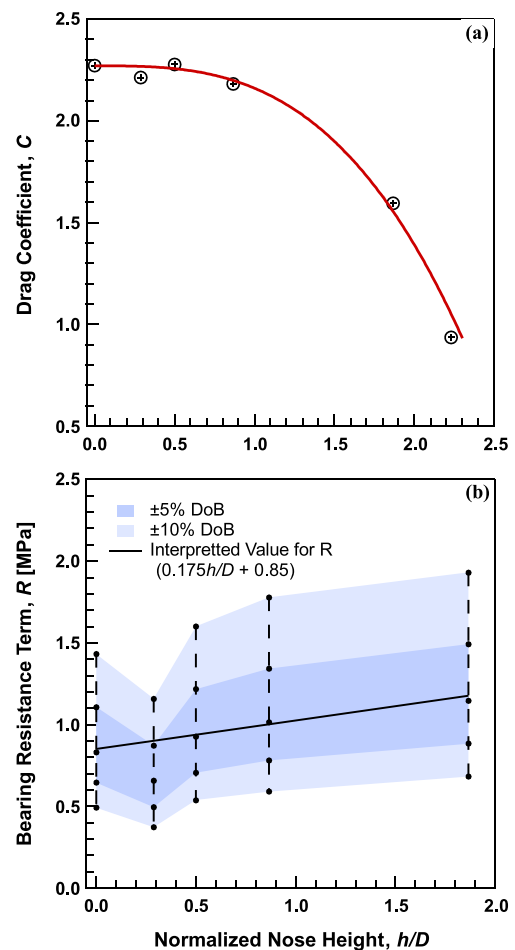


Fig. 16 Drag Coefficient and Bearing Resistance Term versus Normalized Nose Height

used as reference and measurement sources. Optical probes were used to collect the Doppler shifted light reflected from the moving target.

The results of the experiments revealed that (1) A cavity begins to expand around the projectile upon impact onto the soil surface. The soil is in contact with the projectile nose, and separation appears to occur at the end of the nose, with little or no contact of the shank with the soil. (2) Loose and dense sand produce similar cavities, with a cavity rim diameter that is only slightly larger in loose sand compared to dense sand. (3) Boundary effects can be present in high-speed penetration experiments. It was found that a combination of using a diameter ratio of approximately 21 and use of shock-absorbing liner materials inside the soil target chamber effectively reduced the majority of the boundary effects. (4) Soil bulk density plays a major role in the DoB only at higher densities. For the bulk densities tested, a threshold bulk density of approximately 1.65 g/cm³ corresponding to a relative density of 60% was identified below which penetration

resistance and depth of burial (DoB) were not sensitive to penetration soil density. Above this threshold DoB decreased linearly with an increase in bulk density. (5) A mass of comminuted sand forms ahead of the projectile nose during high velocity penetration, known as a false nose. This false nose was approximated as a cone with a 60° apex angle for the soils tested. Projectile nose shape affected penetration only if the nose apex angle was sharper than 60°; blunter projectile noses produced nearly identical results. (6) An incremental Poncelet equation corrected for nose shape predicted the velocity-penetration data with reasonable accuracy. The resulting drag coefficient, C , and bearing resistance, R , varied from 0.93–2.18 and 349–1002 kPa for densities in the range of 1.57–1.82 g/cm³, respectively. Varying the nose sharpness for conical nose from 30–180° resulted in C in the range of 1.59–2.27, and R ranging from 1177–850 kPa, respectively.

An emerging understanding of soil response to high velocity impact and penetration based on the above observations and phenomenological conjectures was presented. High velocity impact into soil results in soil contact stresses that exceed the strength of soil particles, leading to soil particle comminution. These comminuted soil particles coalesce into a densely packed conical mass, adhering to the projectile, and persisting throughout subsequent stages of penetration. Continued supersonic penetration leads to further crushing of soil particles as the stresses surpass the crushing strength of the individual soil particles. As the velocity of the projectile decreases, the stresses imposed on the soil contacts decrease as well, decaying to a critical crushing stress of approximately 25–30 MPa. Beyond this point, particle crushing is somewhat mitigated, and the penetration mechanism shifts from one of crushing-dominated to one where further penetration is facilitated by the outward rearrangement of soil particles.

Acknowledgements The authors gratefully acknowledge the support of the Strategic Environmental Research and Development Program (SERDP) Project No: MR19-1277. A NAC HX5 high-speed camera was used. The authors acknowledge technical support from Quantifi Solutions for the PDV equipment and setup. Launcher operation support was provided by Sydor Technologies.

Data availability All data, models, and code generated or used during the study appear in the submitted article.

References

- Robins, B.: New Principles of Gunnery. Originally published in 1742. In: James W. (ed.) *Mathematical Tracts of the Late Benjamin Robins*, 1, 341 (1761). London
- Poncelet, J.V.: *Introduction à la Mécanique Industrielle*. Brussels. 2nd edn. Meline: Cans et Compagnie. p. 271. (1839)
- Bester, C.S., Behringer, R.P.: Collisional model of energy dissipation in three-dimensional granular impact. *Physical Review E*, **95**(3), 032906 (2017)
- O’Beirne, C., O’Loughlin, C.D., Gaudin, C.: A release-to-rest model for dynamically installed anchors. *J. Geotechnical Geoenvironmental Eng.* **143**(9) (2017). [https://doi.org/10.1061/\(ASCE\)GT.1943-5606.0001719](https://doi.org/10.1061/(ASCE)GT.1943-5606.0001719)
- Kotov, V.L., Balandin, V.V., Bragov, A.M.: Quasi-steady motion of a solid in a loose soil with developed cavitation. *Dokl. Phys.* **58**(7), 309–313 (2013)
- O’Loughlin, C.D., Richardson, M.D., Randolph, M.F., Gaudin, C.: Penetration of dynamically installed anchors in Clay. *Géotechnique*. **63**(11), 909–919 (2013)
- Umbanhowar, P., Goldman D.I.: Granular impact and the critical packing state. *Physical Rev. E*, **82**(1), 010301(R) (2010)
- Clark, A.H., Behringer, R.P.: Granular impact model as an energy-depth relation. *Europhys. Lett.* **101**(6), 64001 (2013)
- Thompson, L.J.: Dynamic penetration of selected projectiles into particulate media. Sandia National Laboratories. Report No. SC-RR-66-376, 212p. (1966)
- Allen, W.A., Mayfield, E.B., Morrison, H.L.: Dynamics of a Projectile Penetration Sand. *J. Appl. Phys.* **28**(3), 370–376 (1957)
- Backman, M.E., Goldsmith, W.: The Mechanics of Penetration of Projectiles into Targets. *Int. J. Eng. Sci.* **16**, 1–99 (1978)
- Forrestal, M.J., Luk, V.K.: Penetration into soil targets. *Int. J. Impact Eng* **12**(3), 427–444 (1992)
- Young, C.W.: Depth prediction for Earth-penetrating projectiles. *J. Soil Mechanics Foundations Div.* **95**(3), 803–817 (1969)
- Taylor, T., Fragaszy, R. J.: Implications of centrifuge penetration tests for use of Young’s equations. In: Clouston L.C. (ed.) *Proceedings of the Fourth International Symposium on the Interaction of Non-Nuclear Munitions with Structures*, Vol 1. Panama City, FL: Air Force Engineering and Services Center. Engineering and Services Laboratory. p 114–118 (1989). Tyndall Air Force Base, Florida
- De Lange, D.: Ontwerp voorschrift bepaling indringingsdiepte conventionele explosieven. Deltares Report No. 1210497-000-GEO-0002, p 28 (2015)
- Bless, S.J., Berry, D.T., Pedersen, B., Lawhorn, W.: Sand penetration by high-speed projectiles. *AIP Conf. Proc.* **1195**, 1361–1364 (2009)
- Borg, J.P., Morrissey, M.P., Perich, C.A., Vogler, T.J., Chhabildas, L.C.: In situ velocity and stress characterization of a projectile penetrating a sand target: Experimental measurements and Continuum Simulations. *Int. J. Impact Eng* **51**, 23–35 (2013)
- Borg, J., Van Vooren, A., Sandusky, H., Felts, J.: Sand penetration: A near nose investigation of a sand penetration event. *Dynamic Behav. Mater.* **1**, 363–371 (2013)
- Omidvar, M., Malioche, J.D., Bless, S., Iskander, M.: Phenomenology of rapid projectile penetration into granular soils. *Int. J. Impact Eng* **85**, 146–160 (2015)
- Thompson, J. B.: Low-velocity impact penetration of low-velocity soil deposits. Ph. D. Dissertation. University of California, Berkeley. (1975)
- Glöbner, C., Moser, S., Külls, R., Heß, S., Nau, S., Salk, M., PenumaduPetricin, D.N.: Instrumented projectile penetration testing of granular materials. *Exp. Mech.* **57**(2), 261–272 (2016)
- Cooper, W.L., Breaux, B.A.: Grain fracture in Rapid Particulate Media Deformation and a Particulate Media Research Roadmap from the PMEE workshops. *Int. J. Fract.* **162**(1–2), 137–150 (2010)
- Ads, A., Iskander, M., Bless, S., Omidvar, M.: Visualizing the effect of fin length on torpedo anchor penetration and pullout using a transparent soil. *Ocean Eng.* **216**, 108021 (2020)

24. Iskander, M., Bless, S., Omidvar, M.: Rapid penetration into granular media: Visualizing the Fundamental Physics of Rapid Earth penetration. Elsevier. (2015)
25. Nordstrom, K.N., Lim, E., Harrington, M., Losert, W.: Granular dynamics during impact. *Physical Rev. Lett.* **112**(22), 228002 (2014)
26. Omidvar, M., Doreau Malioche, J., Chen, Z., Iskander, M., Bless, S.: Visualizing kinematics of dynamic penetration in granular media using transparent soils. *Geotech. Test. J.* **38**(5), 20140206 (2014)
27. Omidvar, M., Iskander, M., Bless, S.: Soil-Projectile Interactions during Low Velocity Penetration. *Int. J. of Impact Eng.* **93**, 211–221 (2016). <https://doi.org/10.1016/j.ijimpeng.2016.02.015>, Elsevier
28. Guzman, I.L., Iskander, M., Bless, S.: A comparison of half and quarter space penetration into granular media. *Geotech. Test. J.* **43**(4), 20190080 (2019)
29. Omidvar, M., Dinotte, J., Giacomo, L., Bless, S., Iskander, M.: Photon doppler velocimetry for resolving vertical penetration into sand targets. *Int. J. Impact Eng.* **185**, 104827. (2024)
30. Peden, R., Omidvar, M., Bless, S., Iskander, M.: Photonic Doppler velocimetry for study of rapid penetration into Sand. *Geotech. Test. J.* **37**(1), 20130037 (2013)
31. Dolan, D.H.: Extreme measurements with photonic Doppler velocimetry (PDV). *Rev. Sci. Instrum.* **91**(5), 051501 (2020)
32. Giacomo, L., Dinotte, J., Omidvar, M.: Resistance of dry and partially-saturated sand to rapid ordnance penetration using photon doppler velocimetry.” In: Rathje, E., Montoya, B.M., Wayne, M.H. (eds.) *Geo-Congress 2023: Geotechnical Characterization (GSP 340)* March 26–29, (2022). Los Angeles, CA
33. Grace, D., Mercurio, S., Omidvar, M., Bless, S., Iskander, M.: A vertical ballistics range with photon Doppler velocimeter instrumentation for projectile penetration testing in soils. *Dynamic Behav. Mater.* **1**, 93–100 (2022)
34. Ao, T., Dolan D. H.: SIRHEN: A data reduction program for photonic doppler velocimetry measurements. Sandia National Laboratories. Report No. SAND2010–3628. (2010)
35. Omidvar, M., Iskander, M., Bless, S.: Response of granular media to rapid penetration. *Int. J. Impact Eng* **66**, 60–82 (2014)
36. Tanaka, K., Watanabe, K., Iwane, K., Fukuma, S., Takayama, K., Kobayashi, H.: Phenomenological studies of the response of granular and geological media to high-speed (Mach 1–5) projectiles. AOARD Final Report, Grant FA2386–10-I-4115, 15p. (2011)
37. Cooper, W. L.: Communication of stresses by chains of grains in high-speed particulate media impacts. In: *Dynamic Behavior of Materials, Volume 1, Proceedings of the 2011 Annual Conference on Experimental and Applied Mechanics.* 99–107. (2011)
38. Goldman, D.I., Umbanhowar, P.: Scaling and dynamics of sphere and disk impact into granular media. *Physical Rev. E.* **77**(2), 21308 (2008)
39. Bolton, M.D., Gui, M.W.: The study of relative density and boundary effects for cone penetration tests in centrifuge. Cambridge University Engineering Department. Technical Report No. CUED/D-SOILS/TR256. (1993)
40. Yankelevsky, D.Z., Feldgun, V.R., Karinski, Y.S.: The false nose shape in a high velocity projectile penetration into Dry Sand. *Int. J. Impact Eng* **177**, 104492 (2023)
41. Collins, A.L., Addiss, J.W., Walley, S.M., Promratana, K., Bobaru, F., Proud, W.G., Williamson, D.M.: The effect of rod nose shape on the internal flow fields during the ballistic penetration of sand. *Int. J. Impact Eng* **38**(12), 951–963 (2011)
42. Lade, P.V., Yamamuro, J.A., Bopp, P.A.: Significance of particle crushing in granular materials. *J. Geotechnical Eng.* **122**(4), 309–316 (1996)
43. Vesić, A.S., Clough, G.W.: Behavior of granular materials under high stresses. *J. Soil Mechanics Foundations Div.* **94**(3), 661–688 (1968)
44. Omidvar, M., Iskander, M., Bless, S.: Stress-strain behavior of sand at high strain rates. *Int. J. Impact Eng* **49**, 192–213 (2012)
45. Børvik, T., Dey, S., Olovsson, L.: Penetration of granular materials by small-arms bullets. *Int. J. Impact Eng* **75**, 123–139 (2015)

Publisher's Note Springer Nature remains neutral with regard to jurisdictional claims in published maps and institutional affiliations.

Springer Nature or its licensor (e.g. a society or other partner) holds exclusive rights to this article under a publishing agreement with the author(s) or other rightsholder(s); author self-archiving of the accepted manuscript version of this article is solely governed by the terms of such publishing agreement and applicable law.